5 Electronic Spectroscopy of the Au-Xe Complex

5.1 Introduction

One of the key questions in chemistry is what constitutes a chemical bond. One answer is to look at intermolecular complexes and to see when a model that is based on a purely physical picture fails, and hence, chemical effects need to be invoked.[1,2,3] A number of investigations have been carried out both experimentally and theoretically (of which three comprehensive reviews exist)[1,4,5] and focus on whether electron density is being shared between the two interacting partners. The interaction between gold cations and rare gases (RG) has proved to be topical with a number of studies published in recent years.[3,6,7,8,9] These studies have provided strong evidence that Au^+-Xe has some element of chemical interaction, contrary to the conclusions of some.[10] It would be advantageous to study this cationic complex experimentally using high resolution photoelectron spectroscopic techniques, with the first step of the employment of these technique being excitation to an intermediate electronic state. Hence, characterization of electronic states of the neutral Au-Xe complex is an important first step to enable the study of the cationic complex experimentally. It has been noted for Au-Ar and Au-Kr in previous chapters that the $D^2\Pi_{1/2}$ and $D^2\Pi_{3/2}$ excited states are considerably more bound than that of the $X^2\Sigma_{1/2}^+$ ground state owing to electron density in the excited states being located off the internuclear axis effectively deshielding the cationic gold core. This

suggests that interactions in the excited states of the neutral Au-Xe complex may resemble those in Au^+-Xe.

In this chapter Au-Xe spectra in the Au $^2P_J \leftarrow {}^2S_{1/2}$ energetic regions are reported. Owing to a number of naturally occurring isomers of Xe[11] [^{128}Xe (1.91%), ^{129}Xe (26.4%), ^{130}Xe (4.1%), ^{131}Xe (21.2%), ^{132}Xe (26.9%), ^{134}Xe (10.4%), and ^{136}Xe (8.9%)] a number of isotopomers of Au-Xe were observed, allowing the absolute vibrational numbering of the progressions to be determined. The results of a number of *ab initio* calculations are also reported that allow accurate determination of spectroscopic constants for the ground state in addition to aiding the interpretation of the complicated spectra obtained.

5.2 Experimental

The experimental procedure has been described in detail in Chapter 2 and so only a brief description of the experiment is outlined here. Au-Xe complexes were generated by pulsing an inert gas (carrier gas Ne or Ar, with a small amount of Xe, ~40% in Ne and ~5% in Ar) held within a mixing volume, over a Au rod held within the LaVa source. Au atoms ablated by the second harmonic of a Nd:YAG laser (Continuum Minilite II) were seeded into the gas pulse which flowed through the cooling channel, before expanding into the high vacuum region of the chamber. The Au-Xe clusters formed in the resulting expansion travelled to the extraction region of the ionization chamber where they were ionized and detected.

During investigations into the Au $^2P_{1/2} \leftarrow {}^2S_{1/2}$ energetic region, Au-Xe complexes were ionized in a (1+1) REMPI scheme by the frequency doubled output of a Sirah dye laser, employing the laser dye Coumarin 540A, focused into the extraction region of the ionization chamber. During investigations into the $^2P_{3/2} \leftarrow {}^2S_{1/2}$ energetic region, Au-Xe complexes were ionized employing a (1+1′) REMPI scheme. The excitation and ionization steps were achieved using the counterpropagating frequency doubled outputs of two Sirah dye lasers. The two dye lasers used the laser dyes Coumarin 480 and Rhodamine B for the excitation and ionization steps respectively. The dye laser used for the single colour experiment and the excitation step in the two colour experiment was pumped by the second harmonic of a Surelite III Nd:YAG laser, whilst the laser used for the ionization step was pumped by the third harmonic from the same laser. As with Au-Kr the voltages on the reppeller plates were adjusted in an attempt to obtain a superior mass resolution with voltages of +1170 V and +1050 V on the lower and upper plate respectively.

5.3 Calculations on Au-Xe complex

Calculations similar to those described in detail in Chapter 3, on the $X^2\Sigma_{1/2}^+$ ground and number of excited states of Au-Ar, were performed for Au-Xe. All calculations were again performed with MOLPRO[12] by other members of the research group.

5.3.1 Au-Xe $X^2\Sigma_{1/2}^+$ state

A potential energy curve for the $X^2\Sigma_{1/2}^+$ state was constructed using single point RCCSD(T) calculations employing the ECP60MDF[13] and ECP28MDF[14] ECP's for Au and Xe respectively. To these ECP's the corresponding *d*-aVXZ-PP (X = Q, 5) basis sets were added. These RCCSD(T) calculations were performed using the frozen core approximation in which only the 5*s* and 5*p* electrons of Xe and 5*d* and 6s electrons in Au were correlated. Each point was corrected for basis set superposition error using the full counterpoise correction, and then extrapolated to the basis set limit using the two point extrapolation procedure of Helgaker and co-workers.[15,16] The potential energy curves were used as input for the LEVEL program[17] as described for Au-Ar. The ^{197}Au and ^{132}Xe isotopes were used for all calculations; the spectroscopic constants determined from these curves are shown in Table 5.1. In addition, an RCCSD(T)/*d*-apwCV5Z single point energy was calculated at the RCCSD(T)/aV5Z R_e value where the inner valence Au electrons were included in the correlation treatment to investigate the effect of core-valence correlation. The 5*s* and 5*p* orbitals of Au overlap with the 4*d* orbitals of Xe so these also need to be included in the correlation treatment; to describe the correlation of these electrons tight functions were added. It is worth noting that the RCCSD(T)/*d*-aCV∞Z calculated dissociation energy of 580 cm^{-1} is in good agreement with the experimental value of 610 ± 3 cm^{-1} obtained recently in a VMI study.[18]

Table 5.1. Calculated spectroscopic constants for ^{197}Au-^{132}Xe $X^2\Sigma^+$

Basis Set	R_e/ Å	D_0'' (D_e'')/ cm^{-1}	ω_e''/ cm^{-1}	$\omega_e''x_e''$/ cm^{-1}
d-aVQZ	3.54	408.9 (419.9)	22.2	0.258
d-aV5Z	3.48	452.8 (464.4)	23.4	0.248
d-apwCV5Z [a]	3.37	519.5 (532.2)	25.2	0.307
d-aV∞Z	3.42	503.1 (515.5)	24.7	0.256
d-aCV∞Z[b]	[3.3]	[580 (590)]	[27]	[0.30]

[a] calculated at the *d*-aCV5Z equilibrium separation.

[b] Estimated from the *d*-aV∞Z values with the change in values between *d*-aV5Z and *d*-apwCV5Z

5.3.2 Au-Xe excited states

The calculations on the excited states of Au-Xe were carried out in a similar manner to those on Au-Ar, which are described in detail in Chapter 3. Initially, curves were calculated from single point, single reference RCCSD(T) calculations employing *d*-aug-cc-pVDZ-PP basis sets, to determine where the states arising from the Au(^2D) + Xe(^1S) asymptote cross the higher lying $^2\Pi$ and $^2\Sigma$ states arising from the Au(^2P) + Xe(^1S) asymptote. The calculated potential curves can be seen in Figure 5.1. As in Au-Ar the states are well separated in energy and the T_1 diagnostic is less than 0.036 suggesting that a single reference method is adequate for the states considered. The most significant result of this calculation is that the states arising from the Au(^2D) + Xe(^1S) asymptote cross the higher lying $D^2\Pi$ states in the bound region. In the Au-Kr complex the crossing occurred just above the bound region of the $D^2\Pi$ states, resulting in the curtailing of the $D^2\Pi_{3/2}$ state spectrum through pre-dissociation. It can therefore be expected that the corresponding Au-Xe spectrum will also exhibit some evidence of this crossing.

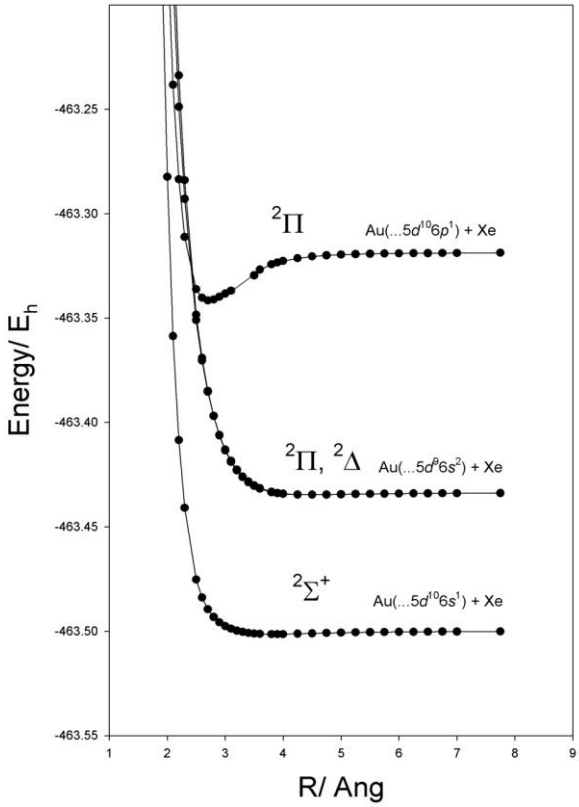

Figure 5.1. Calculated RCCSD(T) potential energy curves for Au–Xe in the absence of spin-orbit interaction. Note that the minimum of the $A^2\Delta$ state lies slightly lower in energy than that of the $B^2\Pi$ state (but this is indiscernible on this scale), and that the $C^2\Sigma^+$ state was omitted from the calculations, but is expected to be essentially identical with the $B^2\Pi$ and $A^2\Delta$ states. The $E^2\Sigma^+$ state was also omitted, but lies above the $D^2\Pi$ state – see Figure 4.2.

Although not initially reported,[19] for comparative purposes the Au-Xe $D^2\Pi$ potential energy curve (which is assumed to represent closely the $D^2\Pi_{3/2}$ state potential) has been subsequently recalculated[20] at the RCCSD(T)/*d*-aVQZ level, performing the full counterpoise correction at each internuclear separation. (Note that the effect of inclusion of SO interaction in the calculations for this state is just expected to shift the $D^2\Pi_{3/2}$ curve up by a constant amount, $\zeta/2$, where ζ is the atomic spin orbit coupling constant for the Au(6^2P) state.) Analysis of this curve yielded R_e' = 2.630 Å, D_e' = 6578 cm^{-1}, ω_e' = 139 cm^{-1} and $\omega_e'x_e'$ = 0.715 cm^{-1}. A single-point RCCSD(T)/*d*-aV5Z at this R_e' value yielded

a D_e' value of 6744 cm^{-1}, which extrapolates to a basis set limit value of 6918 cm^{-1}, which gives a D_0' value of 6849 cm^{-1}.

Further CASSCF + MRCI calculations on the $D^2\Pi$ and $E^2\Sigma^+$ states employing aug-cc-pVQZ-PP basis sets were performed. As with Au-Ar the Davidson-corrected CASSCF + MRCI energies of the two $^2\Pi$ states and the $^2\Sigma^+$ were used as the unperturbed energies in state-averaged CASSCF spin-orbit calculations, to determine the spin orbit coupling at each *R*. The results of a more comprehensive set of calculations, which include these and other states (described later) are shown in Figure 5.2.

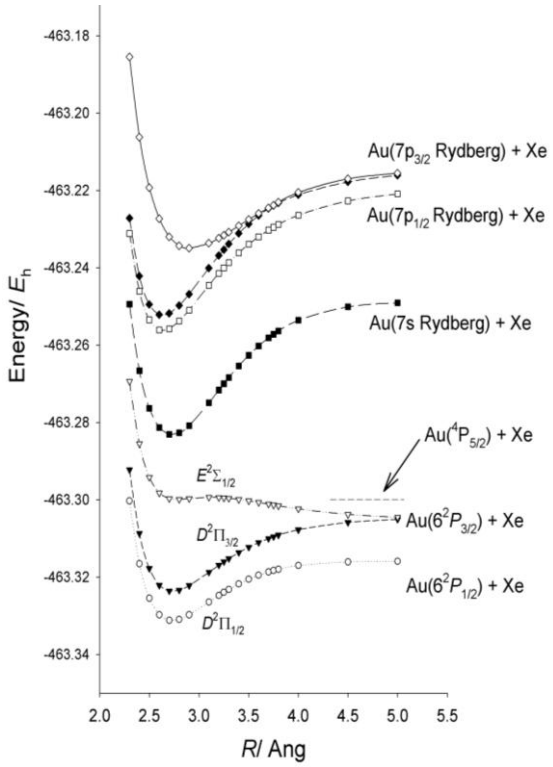

Figure 5.2. CASSCF + MRCI + Q calculations on the excited states of Au–Xe including spin-orbit coupling. The *D* and *E* states arise from the Au – localized $6^2P_J \leftarrow 6^2S_{1/2}$ excitation, the other states correspond to excitation of the Au 6*s* electron to the 7*s* and 7*p* Rydberg orbitals. The position of the Au($^4P_{5/2}$) + Xe($^1S_0$) asymptote has been marked using the experimental value for the Au($^4P_{5/2}$) ← Au ($6^2S_{1/2}$) excitation energy.

It should be noted that additional calculations have been performed for the Au-Xe complex but are not reported in this section. These additional calculations are referred to at the appropriate point to maintain a logical flow in the presented argument.

5.4 Experimental results and discussion

5.4.1 Spectrum in the vicinity of the Au ($6^2P_{1/2}$) atomic transition

Figure 5.3 shows the spectrum obtained for Au-Xe in the region of the Au $^2P_{1/2}$ atomic transition. As can be seen, the spectrum extends over a large energetic region and is red shifted from the Au ($6^2P_{1/2}$) ← Au ($6^2S_{1/2}$) atomic transition[21] which lies at 37358.9 cm^{-1}. The spectrum exhibits a number of broad features at lower energy, a dip in intensity in the centre of the spectrum and then narrower features to the higher energy end of the spectrum. The spectrum in Figure 5.3 was obtained by gating over all of the isotopomers; higher resolution scans, which again were collected by gating over each isotopomer, were obtained for each of the higher energy features (v' = 28 - 32). Figure 5.4 shows the high resolution scan over a 35 cm^{-1} range showing that the positions of the individual isotopomers could be clearly established. As can be seen in Figure 5.3 the lower energy features are considerably broader than those to higher energy, this made an accurate determination of the individual isotopomers in these features considerably more difficult. The maximum of these broader features, which were assigned to be the most abundant isotopomer ^{197}Au-^{132}Xe, in addition to the line positions of the isotopically resolved features are shown in Table 5.2.

Table 5.2. Transition wavenumbers for the $D^2\Pi_{1/2} \leftarrow X^2\Sigma_{1/2}^+$ transition. For $v' = 28–32$ these are isotopomer specific, as noted; for $v' = 16–27$, these are the peak maxima, which are expected to correspond to the $^{197}Au–^{132}Xe$ isotopomer.

v'	$^{197}Au–^{129}Xe$	$^{197}Au^{130}Xe$	$^{197}Au–^{131}Xe$	$^{197}Au–^{132}Xe$
16				*35087.1*
17				*35208.2*
18				*35325.3*
19				*35438.9*
20				*35556.5*
21				*35656.0*
22				*35772.1*
23				*35870.6*
24				*35969.6*
25				*36063.1*
26				*36148.0*
27				*36252.1*
28	36354.9	36349.8	36342.9	36337.0
29	36441.1	36434.0	36249.0	36423.1
30	36524.5	36521.5	36512.4	36506.4
31	36605.4	36599.1	36593.4	36587.3
32	36684.1	36679.3	36672.0	36666.0

Using the same method that was used for Au-Kr, the experimental isotopic shifts between isotopomers of the higher energy features were compared to theoretical shifts to determine the absolute vibrational numbering of the progression. Figure 5.5 (a) – (c) shows the results of these analyses of isotopic shifts. As can be observed, the analysis suggests that the first vibrational level for which all the isotopomers are observed is $v' = 28$. The agreement for the plots shown with $\xi = 28$ is very good, however, three more analyses, in which the ^{197}Au-^{130}Xe line positions were used in conjunction with line positions of the other isotopomers, exhibited considerable scatter. This scattering is a result of an increased error in the measuring of the ^{197}Au-^{130}Xe line positions owing to the significantly lower intensity of the ^{197}Au-^{130}Xe features as can be seen in Figure 5.4.

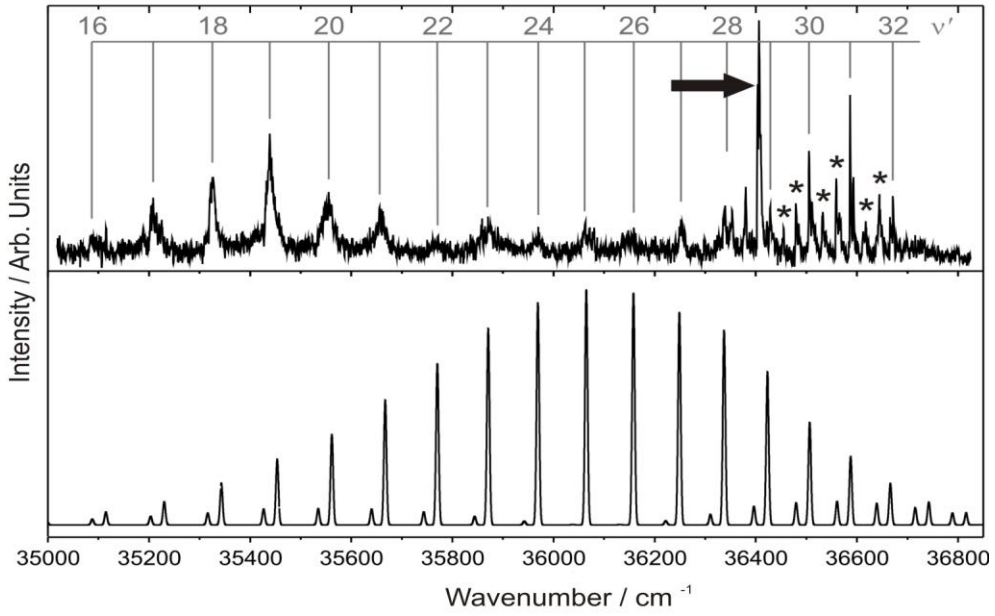

Figure 5.3. Top trace shows the (1+1) REMPI spectrum obtained for the $D^2\Pi_{1/2}$ ← $X^2\Sigma_{1/2}^+$ Au-Xe transition. The spectrum was recorded using a gas mix of 1.5 bar Xe topped up to 3.5 bar with Ne. The absolute vibrational numbering was determined from an isotopic analysis of vibrational features above $v' = 28$ (see text). Hot bands features are marked by an asterisk. The strong feature marked with an arrow does not fit the vibrational progression, and its intensity changed with conditions relative to the other features in the spectrum; it has yet to be assigned. Bottom trace shows Franck-Condon simulation of spectrum

At first glance, the spectrum in Figure 5.3 might be assumed to consist of observed features from two, or possibly three separate progressions, owing to the range of different intensities and widths observed for the features. However in Figure 5.6 it can be observed that the maxima of the lower energy features, expected to be dominated by the ^{197}Au-^{132}Xe isotopomer, fall on the same Morse potential curve as the higher energy ^{197}Au-^{132}Xe features. This indicates that the features are all part of the same progression. The only exception is the feature indicated by an arrow in Figure 5.3, whose relative intensity changed independently of the rest of the spectrum; at present this feature is still unassigned. Considering the

spectrum in light of the evidence that the features are all part of the same vibrational progression, the varying widths of the peaks suggest that there is some υ-dependent predissociation occurring, a point that is discussed later in this chapter.

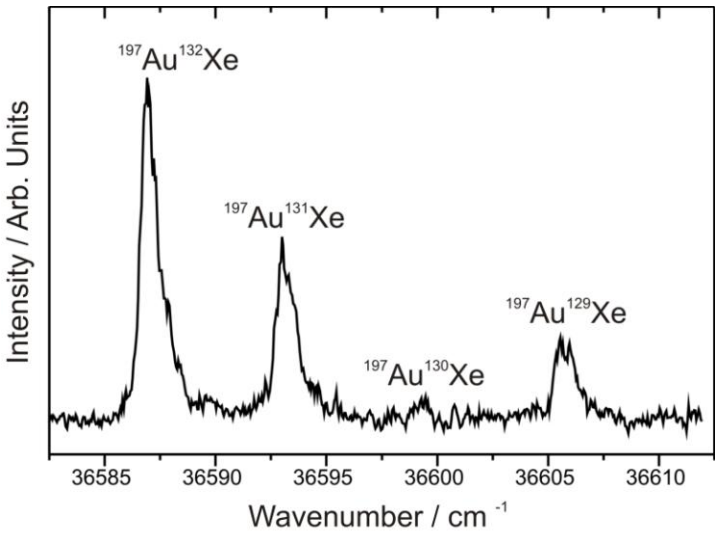

Figure 5.4. High resolution scan over $\upsilon' = 31$ displaying the energy separation of individual isotopomers.

A Morse analysis was carried out for each isotopomer (for $\upsilon' = 28$-32) to derive the spectroscopic constants reported in Table 5.3. Considering the most abundant isotopomer ^{197}Au-^{132}Xe, an expected dissociation limit for the $D^2\Pi_{1/2}$ state of 37939 cm^{-1} can be determined, obtained from the *ab initio* value of D_0''=580 cm^{-1} and the atomic transition energy[21] of 37358.9 cm^{-1}. This suggests that the observed levels in the spectrum are significantly below the dissociation limit, in agreement with the Morse estimate of υ at the dissociation limit of υ_D = 63.4. An estimate of D_0' using the *ab* initio D_0'' value, the atomic transition energy and the $\upsilon' = 0 \leftarrow \upsilon'' = 0$ transition energy, T_0, determined by the Morse analysis yields a value of 5083 cm^{-1}. This value is relatively close to the D_0' value derived directly from the Morse

approximation of 4946 cm^{-1} suggesting that a value of 5020 ± 100 cm^{-1} would be a reasonable estimate for the $D^2\Pi_{1/2}$ state dissociation energy.

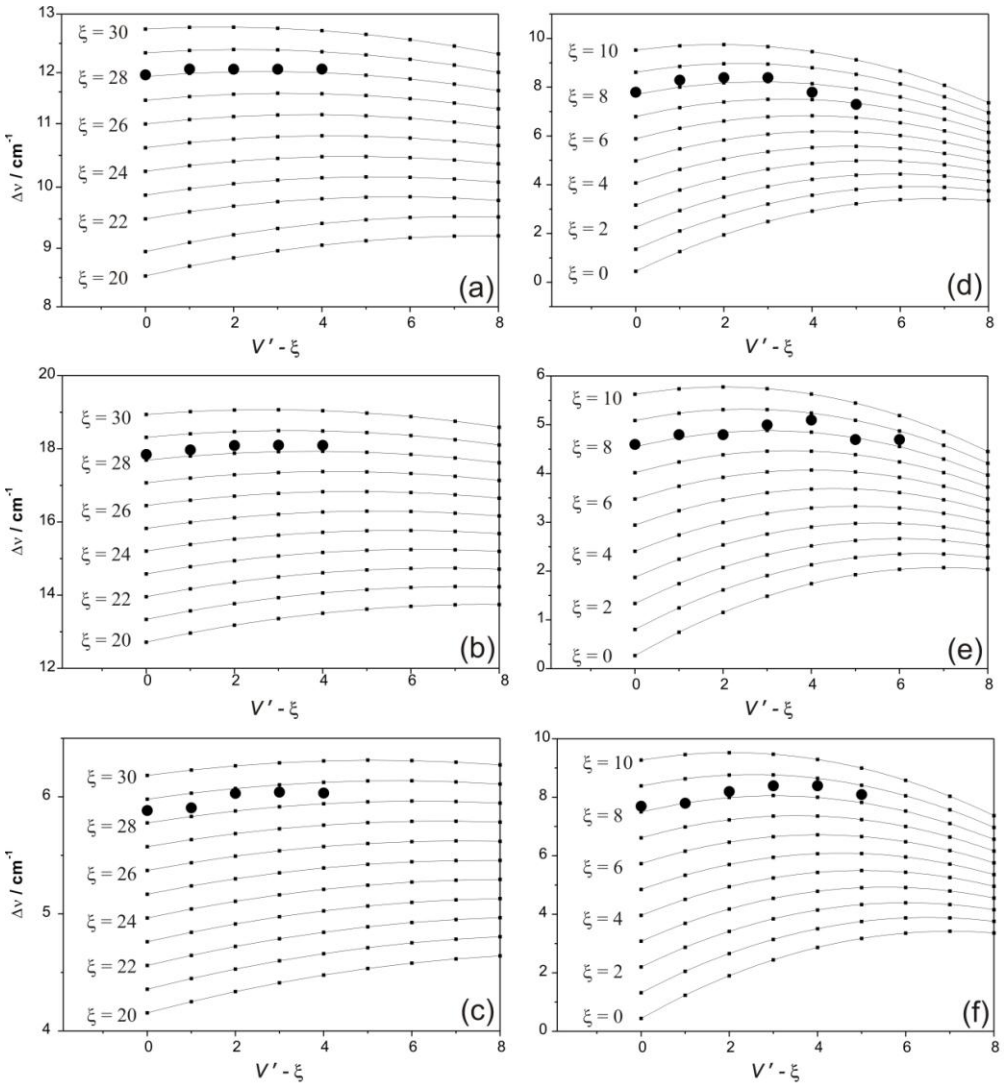

Figure 5.5. Isotopic shift analysis of the features observed for the $D^2\Pi_{1/2} \leftarrow X^2\Sigma_{1/2}^+$ Au-Xe transition (a) – (c) and in the region of the Au ($6^2P_{3/2}$) atomic transition (d) – (e). The larger dots represent the experimental shifts; smaller dots theoretical shifts. ξ represents a running integer variable, allowing theoretical shifts to be compared to experiment.

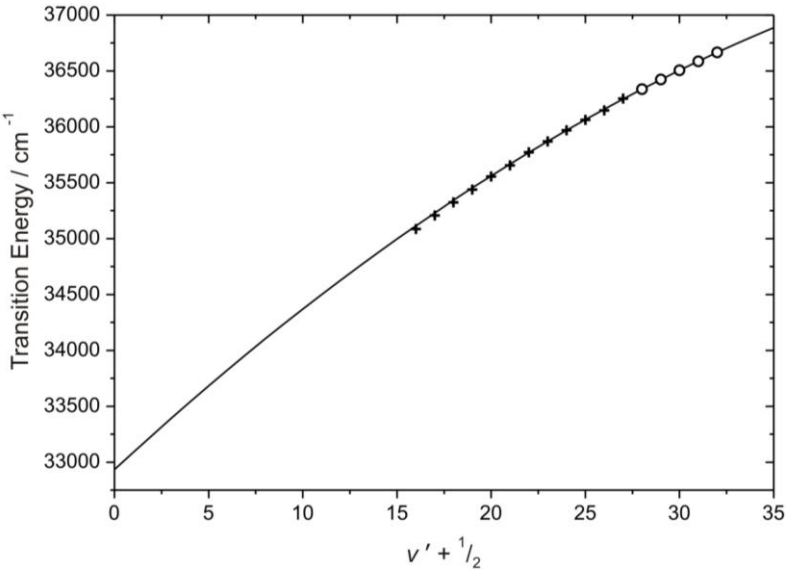

Figure 5.6. The solid line represents the Morse approximation fit for the v' = 28-32 levels of the ^{197}Au-^{132}Xe. The open circles are the energies of these features and the crosses the energies of the v' < 28, indicating that all features are part of the same vibrational progression.

Franck-Condon simulations were carried out for the $D^2\Pi_{1/2} \leftarrow X^2\Sigma_{1/2}^+$ Au-Xe transition. In performing the simulation, efforts were concentrated on matching the intensity of the higher energy features as it was felt that owing to their narrow profile they were the least likely to be affected by predissociation. The simulated spectrum at ΔR = 0.65 Å can be seen in Figure 5.3. It can be observed there is a good agreement between the intensity of the features in the simulated and experimental spectra at low and high energies. However in the central region of the spectrum there is a considerable difference, with the intensity of the experimental features being significantly lower than that predicted by the simulation. Hence, there must be some mechanism by which the central features are losing intensity. As previously mentioned in section 4.3.2 the calculations investigating where the states arising from Au(^2D) + Xe(^1S) asymptote cross the higher lying $D^2\Pi$ states, shown in Figure 5.1, suggest the crossing

point is in the bound region of the $D^2\Pi$ states. It is therefore hypothesized that the states arising from Au(^2D) + Xe(^1S) asymptote could provide a mechanism through which predissociation could occur, a point that will be discussed again later.

Table 5.3. Table of spectroscopic constants derived for the $D^2\Pi_{1/2}$ state (cm^{-1}).

	^{197}Au–^{129}Xe	^{197}Au–^{130}Xe	^{197}Au–^{131}Xe	^{197}Au–^{132}Xe
ω_e'	159.0	160.1	158.1	157.2
$\omega_e'x_e'$	1.258	1.274	1.244	1.230
D_e'	5024.9	5030.8	5025.8	5025.4
D_0'	4945.7	4951.1	4947.0	4947.1
T_0	32846.3	32821.3	32847.6	32855.8

Experimental values for the $v''=0$ - $v''=1$ and $v''=1$ - $v''=2$ spacings 27 ± 2 and 25 ± 2 cm^{-1} respectively were determined from the analysis of hot bands, marked by asterisks in Figure 5.3. As can be seen these are in good agreement with values derived from the "best" theoretical values ω_e'' and $\omega_e''x_e''$ shown in Table 5.1.

5.4.2 Spectrum in the vicinity of the Au ($6^2P_{3/2}$)

Initial scans to the red of the Au($6^2P_{3/2}$) ← Au($6^2S_{1/2}$) atomic transition were carried out based on assumptions from previous work on Au-Ar and Au-Kr that the $D^2\Pi_{3/2}$ origin would be considerably red-shifted from the atomic transition. In reference 19 it was reported that no signal was observed in this spectroscopic region, however, a very recent survey of this region found four isotopically resolved features that appear to correspond to a single vibrational level. The line position of the most intense feature is at 39754.8 cm^{-1}, although, at the time of writing the isotopomer this peak corresponds to is

undetermined. Further scans closer to the atomic transition performed within the original study[19] found a number of features that are shown in Figure 5.7. Again "high resolution" scans were performed over each feature to enable identification of individual isotopomers as shown in Figure 5.8. The line positions of the individual isotopomers are reported in Table 5.4; at lower υ' levels the spacings between the individual isotopomers were sufficiently small that it was challenging to distinguish between them. It should be noted that originally it was assumed, and hence reported,[19] that the maxima of the observed feature would correspond to ^{197}Au-^{132}Xe; however, it now seems likely these maxima actually correspond to the ^{197}Au-^{129}Xe isotopomer,[18] originally and incorrectly labelled as the ^{197}Au-^{130}Xe isotopomer. This discrepancy in the former assignment of the lower energy (υ' = 4 – 7) features is highlighted by comparison of the two Birge-Sponer plots shown in Figure 5.9. It can be seen in Figure 5.9(b), that when the lower energy features are plotted as part of the ^{197}Au-^{132}Xe vibrational progression there is an obvious "kink" in the points of Birge-Sponer plot. This "kink" is not apparent when the features correctly assigned as part of the ^{197}Au-^{129}Xe progression in Figure 5.9(a). The absolute vibrational numbering used in these Birge-Sponer plots was determined through analysis of shifts between the isotopomers, the results of which are shown in Figure 5.5 (d) – (f). As can be seen the shifts are consistent with ξ = 8; analysis of other isotopomers are consistent with this result. However, it should be noted that for analyses involving the ^{197}Au-^{128}Xe isotopomer the plots exhibited considerable scatter, again indicative of the increase in error in determining its line positions.

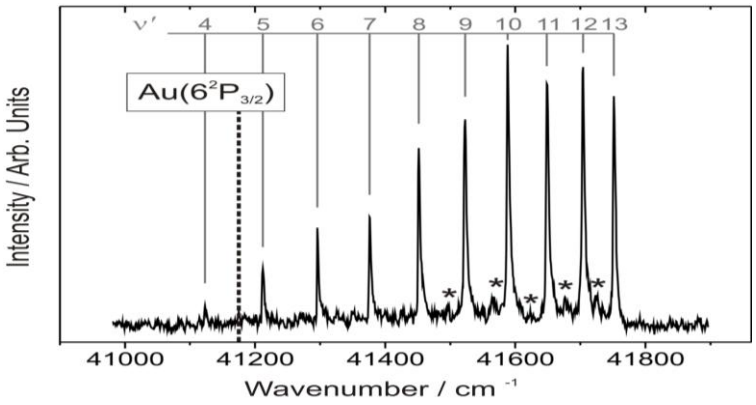

Figure 5.7. (1+1′) REMPI spectrum of Au-Xe $\Xi_{1/2}$ state.

Table 5.4. Table showing ^{197}Au-Xe isotopomer line positions (cm^{-1}) for the $\Xi_{1/2}$ spectrum. For v' = 8-13 these are isotopomer specific as noted in text; for v' = 4-7 the reported position corresponds to the peak maxima suspected to be ^{197}Au-^{129}Xe.[18]

v'	Au–^{128}Xe[a]	Au–^{129}Xe[b]	Au–^{131}Xe	Au–^{132}Xe	Au–^{134}Xe	Au–^{136}Xe
4		*41123.2*				
5		*41211.9*				
6		*41295.9*				
7		*41375.8*				
8	41453.4	41450.9	41447.7	41446.2	41443.1	41440.0
9	41524.3	41520.9	41517.4	41515.8	41512.6	41509.6
10	41590.5	41587.4	41583.8	41582.0	41579.0	41575.6
11	41651.9	41648.1	41644.7	41642.9	41639.7	41636.3
12	41705.2	41702.4	41699.8	41697.9	41694.7	41691.4
13	41753.2	41750.3	41747.7	41746.0	41743.0	41739.6

[a] Originally reported as ^{197}Au^{129}Xe isotopomer.[19]

[b] Originally reported as ^{197}Au^{130}Xe isotopomer.[19]

As before, the derived absolute vibrational numbering enabled a Morse analysis to be performed yielding a number of spectroscopic constants, the results of which are reported in Table 5.5. Considering the most abundant isotopomer, ^{197}Au-^{132}Xe, then combining the values of T_0 and D_0', yields the apparent dissociation limit for this state as 41886.0 cm^{-1}. Comparing this dissociation limit, to one obtained from the addition of the atomic transition with that of the calculated D_0'' (yielding a value of 41754 cm^{-1}), then this could imply

that there is a barrier to dissociation whose height is ≤131 cm^{-1}. It should be noted that the value reported for T_0 in Table 5.5 is revised from that previously reported,[19] hence, the derived values for the apparent dissociation limit and barrier height also differ to those originally reported.

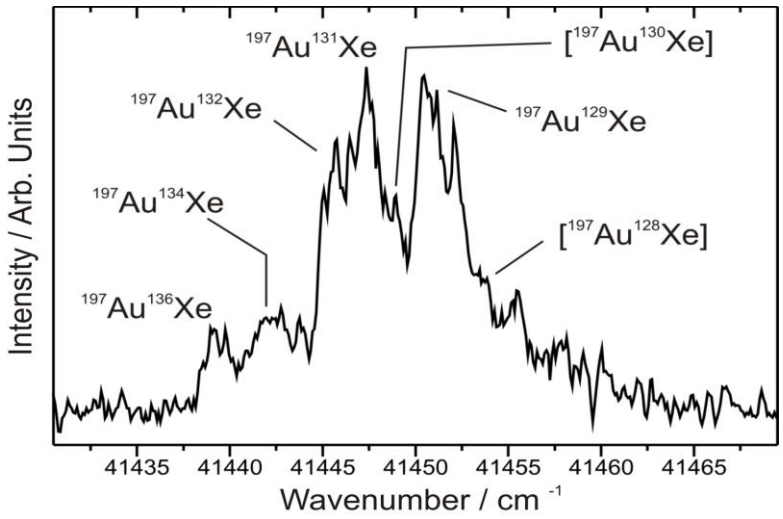

Figure 5.8. High resolution scan over a single vibrational transition (v' = 8) of the spectrum in Figure 5.7, showing the contribution of different isotopomers.

From the analysis of the spectrum observed in Figure 5.7 it has been determined that the absolute vibrational numbering in this state is considerably lower than that observed for the $D^2\Pi_{1/2}$ state and that it is also considerably less bound. From previous work on Au-Ar and Au-Kr (see chapters 3 and 4) and evidence from theoretical calculations it seems very unlikely that the $D^2\Pi_{3/2}$ state would be less bound or have a lower absolute vibrational numbering than the $D^2\Pi_{1/2}$ state. It can therefore be concluded that it is not the $D^2\Pi_{3/2}$ state that is responsible for the spectrum presented in Figure 5.7.

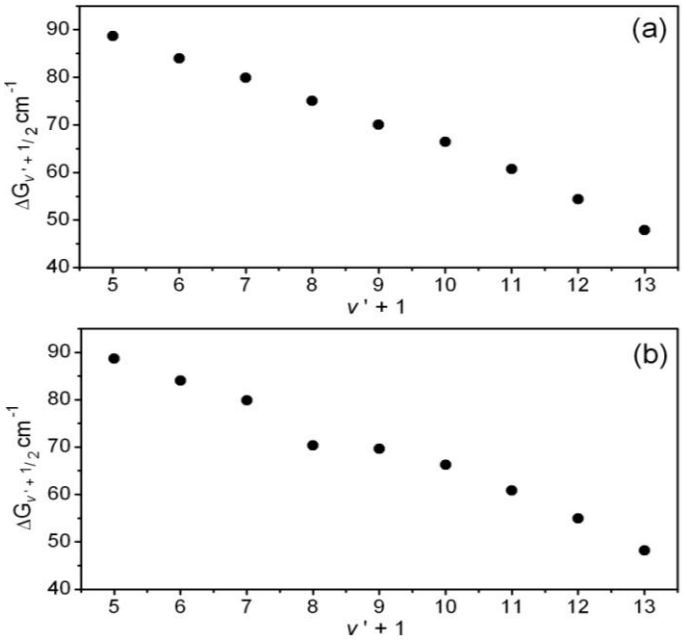

Figure 5.9. Comparison of Birge-Sponer plots when lower energy features (v' = 4 - 7) of $\Xi_{1/2}$ spectrum plotted as part of (a) ^{197}Au-^{129}Xe and (b) ^{197}Au-^{132}Xe vibrational progressions. The "kink" observed in (b) indicates that the features are not part of this vibrational progression.

Considering the location of the observed line position in the most recent study it is a reasonable assumption that it corresponds to the Au-Xe $D^2\Pi_{3/2} \leftarrow X^2\Sigma_{1/2}^+$ transition. The observation of a single vibrational feature is in line with experimental trends observed for previous work and the trends observed for the RCCSD(T) calculations on the excited states. In Au-Ar, a long progression of features was observed for the $D^2\Pi_{3/2}$ state, whilst for Au-Kr a severely reduced progression was observed. Results from RCCSD(T) calculations on these two species suggested that it was the position that states arising from Au(^2D) + RG(^1S) asymptote crossed the respective $D^2\Pi_{3/2}$ state potential that caused the observed difference. In Au-Ar, the calculations suggested that the lower lying states crossed high on the repulsive wall of the $D^2\Pi$ potential while in Au-Kr the crossing was considerably closer to the bound region of the potential. It is

suspected that the progression in the observed Au-Kr $D^2\Pi_{3/2}$ state spectrum was severely narrowed owing to a predissociation mechanism involving the weakly bound $A^2\Delta_{3/2}$ state.

Table 5.5. Table of spectroscopic constants derived for the unassigned Ω=1/2 state (cm^{-1}).

	^{197}Au-^{128}Xe	^{197}Au-^{129}Xe	^{197}Au-^{131}Xe	^{197}Au-^{132}Xe	^{197}Au-^{134}Xe	^{197}Au-^{136}Xe
ω_e	125.2	122.6	120.8	120.1	119.7	119.2
$\omega_e x_e$	2.962	2.844	2.751	2.724	2.705	2.688
D_e'	1323.9	1322.2	1325.2	1324.0	1324.3	1322.8
D_0'	1262.0	1261.6	1265.5	1264.6	1265.1	1263.8
T_0	40602.5	40613.3	40619.3	40621.4	40620.5	40620.1

As can be seen in Figure 5.1 the states arising from Au(^2D) + Xe(^1S) asymptote cross the Au-Xe $D^2\Pi_{3/2}$ state in the bound region of its potential. It can therefore be hypothesized that the Au-Xe $D^2\Pi_{3/2}$ state is even more severely affected than the Au-Kr $D^2\Pi_{3/2}$ state and hence only a single vibronic transition is observed on the timescale of the experiment.

It is clear that the spectrum in Figure 5.7 is not due to that of the $D^2\Pi_{3/2} \leftarrow X^2\Sigma_{1/2}^+$ transition; hence an assignment for the source of this spectrum is required. A possible candidate is the $E^2\Sigma_{1/2}^+ \leftarrow X^2\Sigma_{1/2}^+$ transition; however, calculations presented in Figure 5.2 suggest that in the absence of any additional interactions this state would be too weakly bound to account for the number of vibrational levels observed. It is also suspected that the $E^2\Sigma_{1/2}^+$ state would be blue shifted from the atomic transition whilst the observed spectrum is slightly red shifted. In Figure 5.10 a schematic diagram is presented, which shows the approximate positions of all the states discussed

above, together with a hypothesized dashed curve that represents the state that gives rise to the observed spectrum. As it was deduced that the state has a barrier to dissociation, its minimum must lie below the $E^2\Sigma_{1/2}^+$ state and there must be an interaction between the two states. The origin of the interacting state is discussed below. It should be noted that herein the state giving rise to the spectrum in Figure 5.7 is denoted to be the $\Xi_{1/2}$ state.

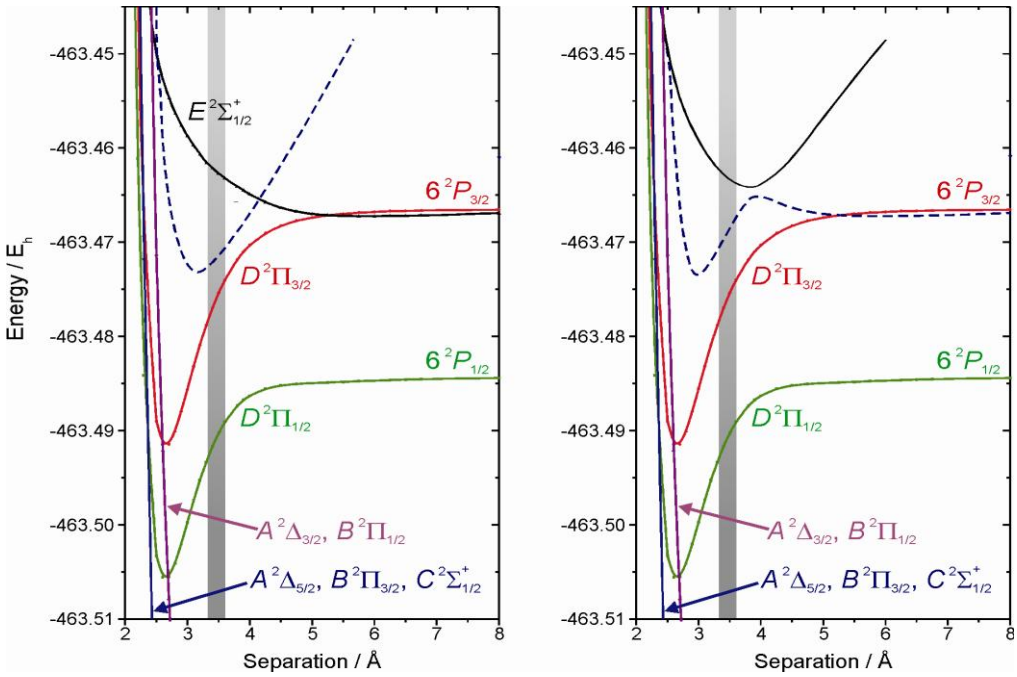

Figure 5.10. Schematic of potential energy curves in the energy region close to the Au 6^2P_J levels. The *A*, *B* and *C* states arise from the Au (^2D_J) + Xe (^1S) asymptotes. These curves are generated by using the RCCSD(T) curves, and shifting them according to the experimental atomic splitting, and assuming the curves are not interacting with any others. The *D* and *E* states are the CASSCF+MRCI+Q curves that have been shifted so that the atomic spin-orbit asymptotes are at the correct energy. The dashed curve represents the state from which the spectrum in Figure 5.7 arises. The left-hand diagram is in the absence of interaction between the dashed curve and the *E* state. The right-hand diagram is in the presence of this interaction. Note the production of a barrier consistent with observations.

5.4.3 Possible involvement of Au—Xe⁺ charge transfer states

The mixing of charge-transfer states into metal dimer excited states has been reported previously in the literature.[22,23,24] It is known that Au has a very large electron affinity (~ 19,000 cm^{-1}),[25] whilst the lowest ionization energies for Xe are 97834 and 108371 cm^{-1} for the $^2P_{3/2}$ and $^2P_{1/2}$ states, respectively. Hence through simple charge calculations of the Coulomb attraction between Au^- and Xe^+ at separations close to the R_e values of the $D^2\Pi_{3/2,1/2}$ states, it is possible to see that a charge transfer (*CT*) state could plausibly be the origin of the observed spectrum. These calculations are only approximate, since they have not taken account of repulsive terms, or higher order ion-induced multipole attractive terms. However, as these terms act in opposite directions, the calculated energies could be a reasonable approximation to that of the charge transfer states. Consequently, states arising from the $Au^- + Xe^+(^2P_{3/2})$ asymptote are expected in this energy region, but states arising from the $Au^- + Xe^+(^2P_{1/2})$ asymptote would be too high in energy. Depending on whether the "*5p*-hole" on Xe^+ is aligned along or perpendicular to the axis, $^2\Sigma_{1/2}^+$ or $^2\Pi_{3/2}$ states will result, denoted as *CT* $^2\Sigma_{1/2}^+$ and *CT* $^2\Pi_{3/2}$. The *CT* $^2\Sigma_{1/2}^+$ state is expected to be the more strongly bound owing to the reduced repulsion along the internuclear axis, because of the Xe^+ "pσ hole"; however both states are expected to be fairly strongly bound, owing to the large Coulomb attractive term.

Given the derived dissociation energy (41886.0 cm^{-1}) for the observed state, it seems unlikely that the reported spectrum can be through the direct observation of the *CT* state, which should be very strongly

bound. However, the *CT* $^2\Sigma_{1/2}^+$ and $E^2\Sigma_{1/2}^+$ states would interact *via* configuration interaction, and this interaction would mix the states. The question then arises as to whether the minimum of the *CT* $^2\Sigma_{1/2}^+$ state is expected to be located above or below the $E^2\Sigma_{1/2}^+$ state. If it were below, then this would imply a curve crossing (or possibly more than one), which in turn might be expected to lead to more complexity than observed in the spectrum. In addition, the spectrum should converge to the Au($^2P_{3/2}$) + Xe($^1S_0$) dissociation limit, and it has been already shown that the convergence point is some way above this energy. The mixing between these states would then be expected to lead to a local minimum close to the R_e value of the *CT* $^2\Sigma_{1/2}^+$ state, with the outer wall rising above the above mentioned atomic asymptote before the curve turns around to converge to this asymptote.

To calculate an accurate position of the *CT* states from high level *ab initio* calculations using the CASSCF + MRCI + Q approach would be challenging, as in contrast to the simplified method for dealing with the Au–Xe states which arise from the Au(6^2P) + Xe(^1S) asymptote, where the 5*d* electrons were kept doubly-occupied for the *CT* states, the 5*d* electrons need to be involved. The reason for this is that the 5*s* and 5*p* orbitals of Xe overlap with the 5*d* orbitals of Au; consequently these orbitals, as well as the Au 6*s* and 6*p* orbitals ought to be included in any CASSCF treatment of these states. In addition, spin-orbit coupling should ideally be included to allow the interaction between the *CT* states and the *D* and *E* state — this would give a total

of twelve spin-orbit states. Owing to the complicated nature of the calculations, to date these calculations have not been performed.

5.4.4 Possible Involvement of Rydberg states

It is also possible that states arising from higher-lying Au asymptotes may be involved, if the binding energy of the complex is high enough. A set of survey CASSCF+MRCI+SO calculations, in which the 5*d* and lower orbitals were kept doubly occupied, were performed; the results are shown in Figure 5.2. As can be seen, it was found that there are states arising from 7*s* and 7*p* Rydberg states of Au in this region, with the state arising from the 7*s* Rydberg asymptote undergoing an interesting configuration interaction with the $E^2\Sigma_{1/2}^+$ state. This interaction results in a local minimum above the dissociation asymptote. However, the interaction is not sufficient to produce the observed spectrum, and in addition is not consistent with the experimentally-derived convergence limit.

5.4.5 Possible involvement of states arising from the Au ($5d^96s^16p^1$) ^4P asymptote

Finally, the possibility that molecular states correlating with the several higher-lying Au($5d^96s6p$) + Xe(^1S) states may be involved is considered. Owing to the d^9 hole, these states are inverted with the lowest level corresponding to the atomic Au($5d^96s6p$, $^4P_{5/2}$) state being at 42164 cm^{-1}, which is only 990 cm^{-1} above the $6^2P_{3/2}$ level and could be involved in the observed spectrum. The Au($5d^96s6p\pi$)–Xe states should be quite similar to the analogous Hg($5d^{10}6s6p\pi$)–Xe excited

states,[26] since the *d* cores of both states will be very small, and the interaction with Xe will involve the large outer shell 6*s* and 6*p*π electrons. Thus, an attractive Ω = ½ state [Au($5d^9 6s 6p\pi$)–Xe] could undergo a Hund's case (c) avoided crossing with the inner repulsive wall of the Au($5d^{10} 6p\sigma$)–Xe, Ω = ½ state, resulting in the final $\Xi_{1/2}$ state bound by ~1100 cm^{-1}. A small outer wall avoided crossing maximum, in the potential curve would be consistent with the results from the Morse analysis that suggested that the dissociation limit lies above the atomic asymptote.

A ^4P atom interacting with a ^1S atom can give rise to $^4\Pi$ and $^4\Sigma^+$ states, in the absence of spin-orbit coupling. When spin-orbit coupling is included, then there are the $^4P_{5/2}$, $^4P_{3/2}$ and $^4P_{1/2}$ states of Au, each interacting with Xe. The molecular states expected are $^4\Pi_{5/2,\ 3/2,\ 1/2,-1/2}$ and $^4\Sigma^+_{3/2,\ 1/2}$. The molecular states of like-Ω will be mixed if Hund's case (c) coupling (or an intermediate case) is considered. It is expected that the states will be inverted, owing to the dominance of the d^9 character. Additionally it is expected that the $^4\Pi_\Omega$ states will lie lower than the $^4\Sigma_\Omega$ ones, since the electron density along the internuclear axis is lower for the Π states. Taking these points into consideration, and applying the non-crossing rule to states of like-Ω, then it can be deduced that there will be a "pure-Π" $^4\Pi_{5/2}$ state lowest in energy, with mixed Π/Σ character in the remaining states, with the $^4\Pi_{3/2}$ and $^4\Pi_{1/2}$ states lying next highest in energy, and each correlating to the Au($^4P_{5/2}$) + Xe($^1S_0$) asymptote; other states will lie higher in energy and correlate to higher atomic asymptotes. Non-counterpoise corrected

RCCSD(T) PEC calculations have been performed on the non-SO $^4\Pi$ state using aug-cc-pVQZ-PP and aug-cc-pV5Z-PP basis sets. Each energy is extrapolated to the basis set limit employing the same method as described above for the $X^2\Sigma_{1/2}^+$ state. This yielded spectroscopic constants determined at the basis set limit of D_0' = 2215.3 cm^{-1}, R_e' = 2.89 Å, ω_e' = 85.5 cm^{-1} and $\omega_e'x_e'$ = 1.15 cm^{-1}. However, these spectroscopic constants will be affected by interaction with the *CT*, Rydberg and Au($5d^9 6s^2$)–Xe states, in a manner which is hard to quantify without detailed mutireference + SO *ab initio* calculations. Therefore the quantities are estimated by analogy with a related system.

The estimated D_0' and R_e' values for the Au($5d^9 6s 6p\pi$)–Xe $^4\Pi$ state are based on similar values for the Hg($5d^{10} 6s 6p\pi$)–Xe $^3\Pi$ states (which have in turn been estimated from experimental spectroscopic results). The Hg–Xe $^3\Pi$ state, which is "pure" Hg($6s6p\pi$)–Xe in nature, has a D_0' value of ~ 1400 cm^{-1} and an estimated R_e' value of ~ 3.1±0.2 Å.[26] If the analogous Au($5d^9 6s 6p\pi$)–Xe state has approximately similar D_0' and R_e' values, and this state correlates to the Au($5d^9 6s 6p$, $^4P_{5/2}$) atomic asymptote at 42164 cm^{-1}, then the state could have its minimum energy near 40750 cm^{-1}, reasonably close to the bound value of ~ 40700 cm^{-1}; the possible states are $^4\Pi_{5/2}$, $^4\Pi_{3/2}$ and $^4\Pi_{1/2}$. Of these the $^4\Pi_{5/2}$ state can be excluded on the grounds that it is not allowed in a single-photon transition from the $X^2\Sigma_{1/2}^+$ state. The $^4\Pi_{3/2}$ state is likely to be coupled to the $D^2\Pi_{3/2}$, and since the latter state is deemed to be fully predissociated in the Franck-Condon window and it can

therefore be assumed that this state will also not be observed. Thus, the most likely candidate for the observed $\Xi_{1/2}$ spectrum is the $^4\Pi_{1/2}$ state mixed with the $E^2\Sigma_{1/2}^+$ state, although the involvement of the *CT* states cannot be excluded.

The schematic diagram in Figure 5.10 shows the proposed avoided crossing, which must result in a small maximum in the resulting lower $\Xi_{1/2}$ potential energy curve, at large *R*, and an ~ 900 cm^{-1} minimum in the lower curve at ~3 Å. The transition to this "mixed" $\Xi_{1/2}$ state will retain some of the $^2P_{3/2} \leftarrow {}^2S_{1/2}$ atomic character, and consequently have some "allowedness" which should vary strongly with *R*. Attempts at obtaining a satisfactory FC simulation of the unusual band intensity distribution exhibited by the spectrum shown in Figure 5.7 were unsuccessful. It is believed that this is partially due to the variation of the electronic transition moment with *R*, and also to the sudden drop off in Franck-Condon intensity to the blue of the $v' = 13$ transition as the energy of the unusual maximum at large *R* in the potential curve is approached.

It should be noted that, although the energy of the cut-off in the spectrum is not coincident with the energy calculated from the *ab initio* D_0'' + atomic excitation energy value, these values are in fairly good agreement. However, it is possible that the calculated value for D_0'' is still slightly too low. It is unclear whether any of the higher-v' levels observed are quasibound or not, but certainly there is no noticeable change in the spectral band width (in contrast to the

observations for the $D^2\Pi_{1/2} \leftarrow X\,^2\Sigma_{1/2}^+$ spectrum). A further discussion of this is given in section 7.3 in light of recent VMI studies.[18]

5.4.6 Mechanism for predissociation of the $D^2\Pi_{3/2}$ and $D^2\Pi_{1/2}$ states

As can be seen from Figure 5.10, the repulsive regions of the $C^2\Delta_{3/2}$ and $B^2\Pi_{1/2}$ potential curves, correlating to the higher Au($^2D_{3/2}$) + Xe($^1S_0$) asymptote, appear to cross both the $D^2\Pi_{1/2}$ and $D^2\Pi_{3/2}$ potential curves in the bound region. As mentioned previously, this would account quite nicely for the single observed $D^2\Pi_{3/2}$ transition, with the other transitions being predissociative on the REMPI timescale, owing to efficient coupling between the repulsive wall of the $C^2\Delta_{3/2}$ and the inner limb of the strongly-bound $D^2\Pi_{3/2}$ state. But, if the $D^2\Pi_{3/2}$ state has pure Au($6s6p\pi$)–Xe character, then the coupling to the $C^2\Delta_{3/2}$ state (if it also has pure Au($5d^96s^2$)–Xe character) should be very weak, since it requires an atomically-forbidden two-electron orbital change [($6p\pi \rightarrow 6s\sigma$) and ($6s\sigma \leftarrow 5d\delta$)]. However, because of the strong spin-orbit coupling of Au, it is known that the atomic Au($5d^{10}6p\ ^2P_{3/2,1/2}$) states have a small amount of Au($5d^96s6p$) character, which can include spin-orbit mixing in of ^4P character.[27,28] This would allow an efficient coupling *via* an allowed one-electron orbital change ($5d^96s6p \leftarrow 5d^96s^2$).

In contrast to the $D^2\Pi_{3/2}$ state, which appears to be completely predissociated, the $D^2\Pi_{1/2}$ state is apparently predissociated in a v'-dependent manner. One tentative possibility for this observation involves consideration of the relative atomic energy spacings of the two

relevant asymptotic $J = {}^1/_2$ states versus the two relevant asymptotic $J = {}^3/_2$ states. The $^4P_{3/2}$ state is 5833 cm^{-1} above the $^2P_{3/2}$ state, while the $^4P_{1/2}$ state is 15838 cm^{-1} above the $^2P_{1/2}$, so that the mixing of $5d^9 6s 6p\ ^4P_J$ character is expected to be much less for the $^2P_{1/2}$ state than for the $^2P_{3/2}$ one.[21] (This is due to the inverted nature of the "*d*-hole" ^4P states, versus the regular nature of the ^2P states.) Consequently, the $D^2\Pi_{1/2}$ state only undergoes relatively slow predissociation (on the REMPI time scale), whereas the $D^2\Pi_{3/2}$ undergoes rapid predissociation, and is not observed. Hence, it can be deduced that states from $v' = 16$–27 overlap those of the repulsive $d^9s^2\ B^2\Pi_{1/2}$ state with maximum probability at ~ $v' = 24$, while the $^2\Pi_{1/2}$ vibrational states with $v' = 28$–32 do not, and so are not markedly predissociated.

5.4.7 Comparison to the cation

It is interesting to compare the results obtained for the Au–Xe complex to earlier results on Au–Kr and Au–Ar, as well as to analogous results reported by Duncan and co-workers on Ag–Ar, Ag–Kr and Ag–Xe.[29] Table 5.6 shows the D_0' values for the $D^2\Pi_{3/2}$ (pure-π) M–RG excited states, as well as previously reported calculated *ab initio* values of D_0^+ for the analogous ground-state M^+–RG complexes.[3] As can readily be seen, the binding energies of the neutral $^2\Pi_{3/2}$ complexes are lower than those of the M^+–RG complexes, as expected, but are still substantial. The final column of the Table lists the $D_0'(^2\Pi_{3/2})/D_0^+(^1\Sigma^+)$ ratios, which are mostly in the 0.5 ± 0.1 range. This is consistent with the view that the perpendicular alignment of the very large and diffuse

excited Au (6$p\pi$) orbital allows the RG atoms to approach the M^+ (d^{10}) core closely, leading to strong physical bonding, which is nonetheless weaker than in the "free" Au^+–RG ions, owing to Au^+ (6$p\pi$)/RG ($np\pi$) repulsion in the neutral states (not present in the free M^+–RG ion ground states).

Table 5.6. D_0 values for the $D^2\Pi_{3/2}$ excited state and $X^1\Sigma^+$ cation states and their ratios.

Species	$D_0(^2\Pi_{3/2})$/ cm^{-1}	$D_0^+(^1\Sigma^+)$/ cm^{-1} [3]	Ratio
Ag–Ar	1199[29]	2539	0.47
Ag–Kr	2267[29]	3815	0.59
Ag–Xe	3630[29]	5801	0.63
Au–Ar	(> 1330)[a]	3669	(>0.36)
Au–Kr	3236	6082	0.53
Au–Xe	(6849)[b,c]	9988	(0.69)[b,c]

[a] CASSCF + MRCI + SO value (From Chapter 3)

[b] Determined from RCCSD(T)/*d*-aV5Z calculations for $D^2\Pi$ state. See text

[c] Values reported are revised[20] from those quoted in published article.[19]

Note, however, that the D_0 ratio for the $^2\Pi_{3/2}$ and $^2\Sigma^+$ ionic states for Au–Xe is anomalously high, near 0.7, since the D_0 value for the $^2\Pi_{3/2}$ state is very high, almost 7000 cm^{-1}. It has previously been postulated[3,6,7,8,9] that the high Au^+–Xe bond energy is indicative of partial "chemical" (coordinate-covalent) bonding, owing to the relativistic stabilization and lanthanide contraction of the formally unoccupied Au^+(6*s*) orbital; therefore it can be postulated that the abnormally high D_0' value for the Au–Xe($D^2\Pi_{3/2}$) neutral state may reflect similar "chemical" effects in the bonding. An additional possibility is that mixing of the strongly-bound Au(7pπ)–Xe $^2\Pi_{3/2}$ Rydberg state character, the position of which is shown in Figure 5.2, into the $D^2\Pi_{3/2}$ state could also increase D_e in the case of Xe, versus Kr.

5.5 Conclusions

REMPI spectra have been presented for the Au–Xe complex obtained in the region of the 6^2P_J states of Au. The lower-energy state can be assigned to the $D^2\Pi_{1/2} \leftarrow X\ ^2\Sigma_{1/2}^+$ transition, but it exhibits a non-Franck-Condon intensity profile. After having established that the features observed in the spectrum were all part of the same vibrational progression, owing to the good description of the energy levels by a Morse potential, the anomalous intensities were explained by indirect coupling with the $C^2\Delta_{3/2}$ state, leading to v-dependent predissociation.

The spectrum observed close to the Au $^2P_{3/2} \leftarrow {}^2S_{1/2}$ atomic resonance was not consistent with an assignment to the $D^2\Pi_{3/2} \leftarrow X\ ^2\Sigma_{1/2}^+$ transition, based upon the low vibrational numbering established and the determined dissociation energy. It is suspected that the spectrum corresponding to this $D^2\Pi_{3/2} \leftarrow X^2\Sigma_{1/2}^+$ transition is severely reduced owing to a predissociation mechanism involving the weakly bound $A^2\Delta_{3/2}$ state resulting in only a single vibrational feature being observed in the expected spectroscopic region.[18]

Various possible assignments of the spectrum observed close to atomic resonance were discussed, some in the light of results from *ab initio* calculations. Although no definitive assignment could be reached, the currently-favoured assignment is to a state arising from a case (c) interaction between the $E^2\Sigma_{1/2}^+$ state and a $^4\Pi_{1/2}$ state, with the latter arising from the Au($^4P_{5/2}$) + Xe($^1S_0$) asymptote; however, the additional involvement of charge-transfer states, which are also

estimated as being likely to appear somewhere in this energy region cannot be discounted. The non-Franck-Condon profile observed can be attributed to the presence of a barrier in the outer wall of the potential curve that gives rise to the spectrum, and subsequent tunnelling/predissociation of states in this energy region corresponding to the barrier, and above.

It is obvious that the spectroscopy Au-Xe complex is complicated and cannot be fully understood by this single REMPI study. In chapter 7 further information from a velocity map imaging study is presented to complement results from this study.

References

[1] D. Bellert and W. H. Breckenridge, *Chem. Rev.*, 2002, **102**, 1595.

[2] W. H. Breckenridge, V. L. Ayles and T. G. Wright, *Chem. Phys.*, 2007, **333**, 77.

[3] W. H. Breckenridge, V. L. Ayles and T. G. Wright, *J. Phys. Chem. A*, 2008, **112**, 4209.

[4] M. A. Duncan, *Annu. Rev. Phys. Chem.*, 1997, **48**, 69.

[5] C. Crépin-Gilbert and A. Tramer, *Int. Rev. Phys. Chem.*, 1999, **18**, 455.

[6] P. Pyykkö, *J. Am. Chem. Soc.*, 1995, **117**, 2067.

[7] D. Schröder, H. Schwarz, J. Hrusák and P. Pyykkö, *Inorg. Chem.*, 1998, **37**, 624.

[8] L. Belpassi, I. Infante, F. Tarantelli and L. Visscher, *J. Am. Chem. Soc.*, 2008 **130**, 1048.

[9] T. Zeng and M. Klobukowski, *J. Phys. Chem. A*, 2008, **112**, 5236.

[10] J. P. Read and A. D. Buckingham, *J. Am. Chem. Soc.*, 1997, **119**, 9010.

[11] http://physics.nist.gov/PhysRefData/Handbook/Tables/xenontable1.htm

[12] MOLPRO is a package of *ab initio* programs written by H. J. Werner, P. J. Knowles and others.

[13] D. Figgen, G. Rauhut, M. Dolg, and H. Stoll, *Chem. Phys.*, 2005, **311**, 227.

[14] K. A. Peterson and C. Puzzarini, *Theor. Chem. Acc.,* 2005, **114**, 283.

[15] T. Helgaker, W. Klopper, H. Koch and J. Noga, *J. Chem. Phys.*, 1997, **106**, 9639.

[16] A. Halkier, T. Helgaker, P. Jỳrgensen, W. Klopper, H. Koch, J. Olsen and A. K. Wilson, *Chem. Phy. Lett.*, 1998, **286**, 243.

[17] R. J. LeRoy, LEVEL 7.2 - *A computer program for solving the radial Schrödinger equation for bound and quasibound levels, and calculating various expectation values and matrix elements*. (University of Waterloo Chemical Physics Research Program Report CP-555R (2000)).

[18] W. S. Hopkins, A. P. Woodham, S. R. Mackenzie, R. J. Plowright and T. G. Wright, *J. Chem. Phys.*, submitted.

[19] R. J. Plowright, M. J. Watkins, A. M. Gardner, C. D. Withers, T. G. Wright and W. H. Breckenridge, *Phys. Chem. Chem. Phys.,* 2009, **11**, 1539-1550.

[20] R. J. Plowright, M. J. Watkins, A. M. Gardner, C. D. Withers, T. G. Wright, M. D. Morse and W. H. Breckenridge, *J. Phys. Chem. A*, 2010, **114**, 9, 3103.

[21] http://physics.nist.gov/PhysRefData/Handbook/Tables/goldtable5.htm

[22] G. A. Bishea, N. Marak and M. D. Morse, *J. Chem. Phys.*, 1991, **95**, 5618.

[23] G. A. Bishea, J. C. Pinegar and M. D. Morse, *J. Chem. Phys.*, 1991, **95**, 5630.

[24] G. A. Bishea and M. D. Morse, *J. Chem. Phys.*, 1991, **95**, 5646.

[25] H. Hotop and W. C. Lineberger, *J. Phys. Chem. Ref. Data*, 1985, **14**, 731.

[26] K. Yamanouchi, J. Fukuyama, H. Horiguchi, S. Tsuchiya, K. Fuke, T. Saito and K. Kaya, *J. Chem. Phys.*, 1986, **85**, 1806.

[27] D. M. Gruen, S. L. Gaudioso, R. L. McBeth and J. L. Lerner J. *Chem. Phys.*, 1974, **60**, 89.

[28] D. Roser, R. Pellow, M. Eyring, M. Vala, J. Lignieres and J. C. Rivoal, *Chem. Phys.*, 1992, **166**, 393.

[29] L. R. Brock and M. A. Duncan, *J. Chem. Phys.* 1995, **103**, 9200.